

Structure and properties of amorphous uranium dioxide

Middleburgh, Simon; Lee, Bill; Rushton, Michael

Acta Materialia

DOI:

[10.1016/j.actamat.2020.10.069](https://doi.org/10.1016/j.actamat.2020.10.069)

Published: 01/01/2021

Peer reviewed version

[Cyswllt i'r cyhoeddiad / Link to publication](#)

Dyfyniad o'r fersiwn a gyhoeddwyd / Citation for published version (APA):

Middleburgh, S., Lee, B., & Rushton, M. (2021). Structure and properties of amorphous uranium dioxide. *Acta Materialia*, 202, 366-375. <https://doi.org/10.1016/j.actamat.2020.10.069>

Hawliau Cyffredinol / General rights

Copyright and moral rights for the publications made accessible in the public portal are retained by the authors and/or other copyright owners and it is a condition of accessing publications that users recognise and abide by the legal requirements associated with these rights.

- Users may download and print one copy of any publication from the public portal for the purpose of private study or research.
- You may not further distribute the material or use it for any profit-making activity or commercial gain
- You may freely distribute the URL identifying the publication in the public portal ?

Take down policy

If you believe that this document breaches copyright please contact us providing details, and we will remove access to the work immediately and investigate your claim.

Structure and properties of amorphous uranium dioxide

Simon C. Middleburgh¹, William E. Lee^{1,2} Michael J.D. Rushton¹

¹Nuclear Futures Institute, Bangor University, Bangor LL57 1UT, United Kingdom

²Department of Materials, Imperial College London, London, SW7 2AZ, United Kingdom

Abstract

Amorphous uranium dioxide (UO₂) has been modelled on the atomic scale using a combination of quantum mechanical (density functional theory) and classical forcefield methods (molecular dynamics and reverse Monte-Carlo). The atomic scale structure of the amorphous state has been predicted and is presented in the form of simulated X-ray diffraction patterns, pair correlation functions and bond angle distributions. These are shown to be consistent with the experimental patterns previously reported. To enable accurate calculation of the energies and magnetic properties, using quantum mechanics, reverse Monte-Carlo was used to generate reduced cells from larger molecular dynamic melt-quenches. This allowed density functional theory energy minimisation for structures consistent with the amorphous state. Building on this, the material's propensity to deviate from stoichiometry, the magnetic structure and amorphous UO₂ surface energy were computed. Non-stoichiometry is accommodated more readily in the amorphous system than in crystalline UO₂. This indicates that deviations from stoichiometry in fuel (for example as a result of operation) will be accommodated at amorphous phases, if present, leaving a more stoichiometric bulk phase – impacting processes including fission gas mobility, melting points and a number of other safety relevant properties. The magnetic structure of bulk amorphous UO₂ is predicted to be a spin-glass, unlike crystalline UO₂ which has anti-ferromagnetic ordering at 0 K. The surface energy of amorphous UO₂ is computed to be 0.79 Jm⁻², which is similar to the experimentally observed surface energy of grain boundary bubbles in UO₂ and comparable to the surface energies reported for crystalline UO₂. Results are pertinent to ongoing efforts to understand the nature of grain boundaries in nuclear fuels, to model fission gas release from them, radiation induced amorphization and the impact of dopants and impurities on nuclear fuel's manufacture and in-reactor behaviour.

Keywords: Amorphous, uranium dioxide, atomic scale simulation, structure, nuclear fuel.

1. Introduction

Uranium dioxide remains the leading nuclear fuel material globally owing to its relative ease of manufacture, stability under normal and off-normal operating conditions, extremely high melting point and benign reactions with the various nuclear reactor coolants currently in use – especially within water-based reactors. Looking forward, UO₂-based fuels are being considered in a number of advanced technology fuel concepts – from increased enrichment (>5 wt.% ²³⁵U) of standard UO₂ pellets, doped UO₂ pellets (common dopants include Cr₂O₃ [1], alumino-silicates [2] and TiO₂ [2] [3]) and the more advanced UO₂-composite fuels, whereby UO₂ is combined with phases that have higher thermal conductivity and/or higher uranium density to improve fuel cycle costs and in reactor performance, for example: uranium mononitride [4] and beryllium oxide [5].

Uranium dioxide is stable to high temperatures and importantly its dimensional stability under severe irradiation is acceptable and predictable. A key property that dictates this dimensional stability is the ability to accommodate radiation damage without bulk amorphization under reactor operating conditions. Still, amorphous UO₂ has been observed and studied experimentally to investigate basic properties of the material as well as ex-reactor behaviour and potential dissolution reactions within spent nuclear fuel. Matzke *et al.* produced UO₂ thin films through an electron beam deposition method and showed that above ~675°C, amorphous UO₂ began to precipitate into a polycrystalline material (providing a ratio between this temperature and the material's melting temperature of ~0.3) [6]. Bruno *et al.* [7] produced an X-ray amorphous UO₂ solid by precipitation from acidic U(IV) perchlorate solution – producing a green solid – highlighting its high solubility of the material in pH 6-10 solutions compared to crystalline UO₂.

Grain boundaries in ceramics are known to exhibit far greater disorder and more open structures than the bulk material. The open structures make them attractive sites for extrinsic species to segregate to, potentially opening them even more [8] [9]. Neat, low complexion grain boundaries are not common when fuel is manufactured. Instead, highly complex grain boundaries or grain boundary phases are formed that are expected to behave distinctly from the bulk material. Recently, Nerikar *et al.* used a combination of experimental methods to identify that the most common grain boundary observed in UO₂ is not described by coincident site lattice (CSL) theory [10] (84.3 % of boundaries) and are instead highly disordered regions. Similar works by Ksibi *et al.* [11] and Bourasseau *et al.* [12] give the fraction of non-CSL boundaries to be similar: 85.44% and 85.1% of the grain boundaries measured, respectively.

In commercial nuclear fuels, largely insoluble dopants such as chromia (Cr₂O₃), alumina (Al₂O₃) and silica (SiO₂) are added to UO₂, well beyond their solubility limits, to produce larger grain sizes during sintering, and in the case of alumina-silica additive fuel, improve the in-reactor behaviour of the pellet too (by increasing grain boundary creep and fission gas retention). It is expected that the grain

boundary phases are highly complex in nature. Soloman *et al.* [13] showed that even small amounts of insoluble impurities (e.g. <50 ppm Si/Fe) could have large consequences on the grain boundary behaviour in UO₂. At temperatures above 1200°C, it was concluded that diffusion within a glassy grain boundary phase accelerates grain interchanges in addition to acting as getters for other impurities that can act to pin grain boundaries. Importantly, below 1200°C, it was concluded that the glassy grain boundary phase controls the creep rate of the material. In the Dillon-Harmer categories for complexions [9], these grain boundaries can be described as either nano-layers or wetting grain boundaries that are structurally disordered. As such, their behaviour can begin to be understood through the modelling of bulk amorphous systems.

Amorphous materials have been modelled atomistically predominantly through use of classical descriptions of atomic bonding [14] [15] [16]– enabling the simulation of many thousands of atoms at a time providing a statistically significant sample of the random glassy/amorphous state (Desai *et al.* [16] specifically investigating amorphous grain boundary behaviour). One such study by Qin *et al.* [17] determined the thermal conductivity of amorphous UO₂ using the same interatomic potential as used here [18]. They determined the lattice contribution to the thermal conductivity to be consistently low $\sim 1.5 \text{ Wm}^{-1}\text{K}^{-1}$ between 200 K and 1500 K. Only recently have more chemically descriptive methods such as density functional theory (DFT) been used to model amorphous structures [19] [20] [21] [22] [23] [24] [25]. Many DFT-based studies have been reported in the related bioactive glass community through cluster descriptions of the system, for example Laurence and Hillier [26], including using supercell approaches similar to the present work [27] [28] [29] and in other glass systems [30] [31]. A number of previous works have used ab-initio molecular dynamics (AIMD) to perform the melt-quench routine to produce the amorphous structure (for example [19] [20]), while others have used an initial randomised structure that is then subsequently relaxed using geometry optimization within various DFT packages [32] [33] and were able to report results consistent with experiments and make useful predictions. The size of the cells used to approximate the amorphous systems in these cases is small (often <100 atoms) and therefore care must be taken to understand the steric effects of the system sizes and initial densities chosen. The quenches performed in previous DFT studies were fast compared to those carried out by classical approaches due to the computational expense (although still faster than what is achieved experimentally). Additional complications such as inclusion of spin-orbit coupling and the consideration of actinide compounds adds to this prohibitive computational effort of AIMD melt-quench studies. The coupling of DFT with the classical description reduces some of these uncertainties but is reliant on a robust classical description of the system. Previous work has shown changes associated with the AIMD approach and the hybrid classical-DFT approach in amorphous ZrO₂ [34].

In this work, we model amorphous UO₂ using a combination of atomic scale approaches: empirical potential models and the more rigorous but computationally-expensive DFT approach in combination

with each other. The phase's propensity to deviate in oxygen stoichiometry is investigated and the structure of the amorphous UO_2 is discussed. Additionally, the magnetic properties are explored as well as a first attempt at computing a value for the amorphous phase's surface energy, a key value in predicting the evolution of the material in reactor.

2. Methodology

Amorphous UO_2 simulation cells containing 96 atoms were created using the same methodology employed by the authors to study amorphous ZrO_2 [34]. This involves using molecular dynamics (MD) to perform simulated melt-quenches to produce large cells which contained 96000 atoms in the stoichiometric case, predicting the structure of amorphous UO_2 . The high computational demands of DFT mean that much smaller systems than this are necessary for quantum mechanical calculations. Consequently, twenty distinct amorphous configurations were generated using the reverse Monte-Carlo (RMC) algorithm [35] each containing 96 atoms for further evaluation using DFT. These were obtained by using RMC to fit structures to O-U, O-O and U-U partial pair correlation functions (see Figure 2), densities and the bond angle distributions (Figure 5) extracted from the MD melt quenched structures.

The details of the combined MD melt-quench and RMC procedure used here are given in our previous paper on amorphous ZrO_2 [34], however some slight variations were made to suit the current system. The classical potential model developed by Cooper, Rushton and Grimes [18] for actinide oxides was used to describe interatomic forces during MD for which a more recent version of the LAMMPS code (16 Mar 2018 version) was used. Additionally, the melt quenches for oxygen excess non-stoichiometry (see below), required the application of a hydrostatic pressure of 9 GPa to obtain a condensed phase during the initial stages of the melt-quench ($T > 2500\text{K}$). This was applied through the Nosé-Hoover barostat used during MD calculations with its pressure being reduced linearly with temperature until it was zero at $T = 2500\text{K}$.

A series of test calculations were also performed to establish whether the RMC step could be avoided when producing small cells for DFT calculation. For these, MD melt-quenches were conducted for simulation boxes containing between 96 and 96000 atoms. These had the same number of atoms as equivalent $n \times n \times n$ UO_2 super-cells where $n = 2, 3, 4, 6, 8, 10$ and 20. The intention of this was to establish if a representative amorphous structure could be obtained by quenching directly into a small box. The results of these tests can be seen in Figure 1 which shows how the radial distribution functions (RDFs) were affected by system size. The systems containing 324 or more atoms show amorphous structures consistent with the largest system size considered (96000 atoms). However, the smallest systems have RDFs demonstrating recrystallisation. This is particularly apparent in the 96 atom case (topmost in Figure 1) which has sharp peaks consistent with the atomic spacing found in fluorite. Similarly,

examination of the 324 atom structure showed a number of nano-crystallites with the fluorite structure, again this is evidenced by the clear long-range order in its RDF.

The tendency for amorphous structures to recrystallise during simulations is greatly enhanced in these smaller systems, this difficulty can be avoided through the use of the RMC method as employed here. This is demonstrated by the bottom RDF in Figure 1 which was produced using this approach. Even though the constituent system still only contains 96 atoms (the same number as in the fully recrystallised structure used in the direct MD quench) the average of the twenty simulation cells, gives pair-correlations that are almost entirely consistent with those of the much larger MD quenched structures.

The twenty cells produced using RMC were structurally relaxed using the Vienna Ab-initio Simulation Package (VASP) [36] under constant pressure. The generalised gradient approximation exchange correlation as described by Perdue, Burke and Ernzerhof (GGA-PBE) [37] was used for all simulations using the supplied projector augmented wave (PAW) library [38]. Spin polarisation effects were considered – both collinear and non-collinear. For both collinear and non-collinear calculations, three types of magnetic ordering were considered before electronic and structural relaxation: no magnetic moment on each uranium, a ferromagnetic type order (potentially favouring an asperomagnetic ordering in the non-collinear system) and an anti-ferromagnetic-like ordering in the amorphous structures (randomised). In the non-collinear simulations, a randomised order was also investigated with $1 \mu_B$ magnitude on each U atom (i.e. initialising the magnetic order to be speromagnetic). The same ordering was produced at the end of the electronic and structural optimisations despite the initial magnetic ordering for each collinear (ferromagnetic) and non-collinear (speromagnetic) calculation – see Section 3.3.1. For all calculations, a Hubbard correction was applied to the U f-electrons ($U=4.50$ eV and $J=0.51$ eV, consistent with previous work on crystalline UO_2 [39]) using the rotationally invariant description as described by Liechtenstein *et al.* [40].

Subsequently, non-stoichiometric supercells were created through the same methodology and lattice energies obtained through DFT, enabling the propensity of the amorphous UO_2 system to accommodate deviations in O:U ratio to be gauged. O_2 gas was taken as the reference energy for these calculations, having proven reliable in previous studies in related systems [34] [41] [42] [43].

Surface energies were also calculated for the stoichiometric amorphous phase by applying a series of vacuum slabs derived from the relaxed DFT systems. For each cell two free surfaces were created by adding a 30 \AA gap above a cutting plane placed normal to the cell's z-axis. In crystalline systems low energy surfaces are typically obtained by cleaving the system along low index crystallographic planes. Without clearly defined atomic layers of this kind, the correct place to cleave amorphous systems is less obvious. Consequently, a simple but effective, search algorithm was used to identify low energy

surfaces. This used the potential model initially used for the MD melt-quenches as it afforded very rapid energy evaluations allowing a brute-force approach to be adopted where it was possible to energy minimise the surfaces obtained by cleaving at every one of the distinct z-coordinates defined by the atomic positions in the system. In this way, a low energy xy cleavage plane was identified for each of the twenty, 96 atom cells. Following surface creation, ten of the vacuum slabs were further evaluated using DFT energy minimisation to obtain the surface energies reported. It should be noted that before making the vacuum slabs, each system was duplicated along its z-axis to create a double height system. This was to ensure the atoms at the centre of the slabs were sufficiently distant from the surfaces to still represent the bulk amorphous structure. As a result, DFT surface calculations contained 192 atoms.

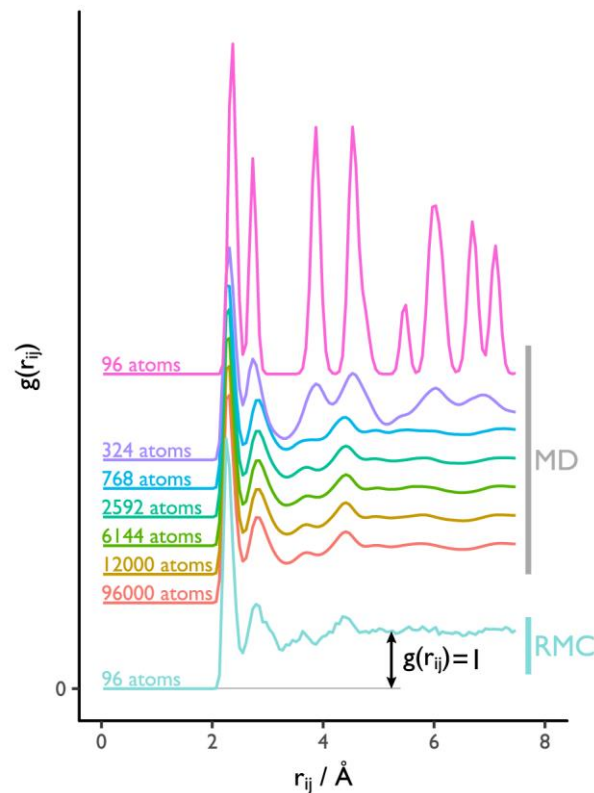


Figure 1 Radial distribution functions obtained from MD melt-quenches performed to show the effect of different system sizes on the resultant structure (displaced along the y-axis for ease of viewing). The smaller systems show clear evidence of recrystallisation; the 96 atom system (top) has fully recrystallised and the 324 atom configuration shows additional peaks consistent with the fluorite structure. The bottommost RDF was obtained using Reverse Monte-Carlo process and has produced a structure consistent with the 96000 atom quench even for the small system size. To allow comparison, RDFs have been displaced vertically but all use the same vertical scale.

3. Results

3.1 Structure

In a similar manner to previous work modelling amorphous ZrO_2 [34], amorphous UO_2 can be described as an edge-sharing structure. This is not unexpected given the fluorite structure is common to both UO_2 and cubic ZrO_2 . It can be seen (Figure 2) that an amorphous structure has been produced with the $g(r_{ij}) > \sim 10 \text{ \AA}$, tending towards 1. The U-U ordering persists to a larger distance than other pairwise bonding in the system, with the O-U bonding shows the least ordering as a function of distance.

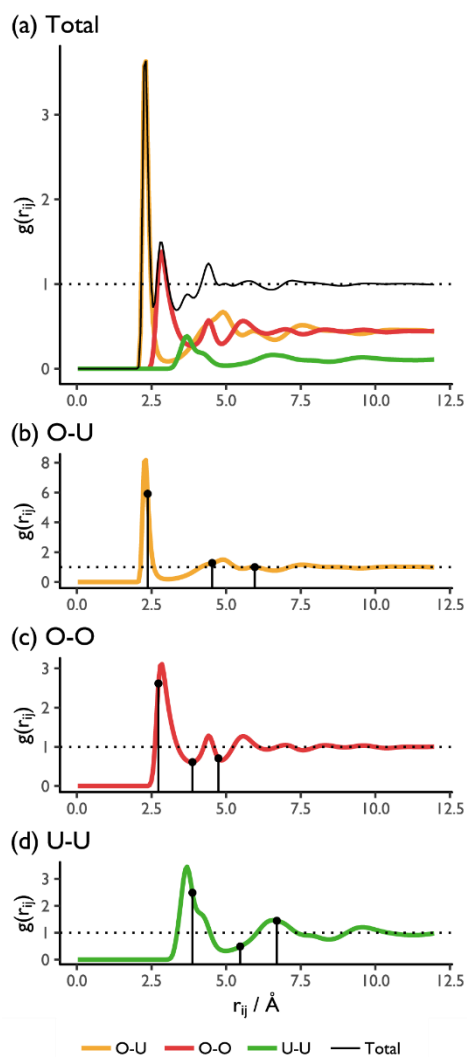


Figure 2 - Pair correlation functions for amorphous UO_2 ; (a) shows the total radial distribution function with the relative contributions of the individual pair correlation functions, (b)-(d) give the individual pair functions. For reference, drop-lines are provided showing the first, second and third nearest neighbour separations for a fluorite crystal equilibrated at the same temperature ($T=300\text{K}$). These data are for the MD melt-quenched system.

The structure produced through the combination of the 20 DFT relaxations (the grey data in Figure 3) were in extremely good agreement with the original MD structures (the blue line in Figure 3), indicating that the MD to DFT methodology is consistent in this respect – the radial distribution function for stoichiometric UO_2 and non-stoichiometric UO_{2+x} and UO_{2-x} is reported in Figure 3 - Radial distribution functions derived from RMC+DFT optimised cells at three different levels of stoichiometry. The dark grey line shows the RDF obtained as the mean and the surrounding, light grey halo, indicates one standard deviation above and below for the 20 individual DFT configurations for each atomic separation and stoichiometry. For comparison, the blue line is the equivalent molecular dynamics melt-quenched system. When non-collinear effects were considered (where the magnetization is treated as a vector instead of a scalar), the systems were found to be lower in energy than the collinear calculations (by 0.96 eV per atom) and therefore non-collinear values are used in all subsequent results unless stated (the magnetic ordering is considered more fully in section 3.3.1). Small deviations from stoichiometry are considered in this work – the density functional theory cells produced from corresponding non-stoichiometric MD melt-quenched structures contained 32 U and 65 O atoms for UO_{2+x} (producing $\text{UO}_{2.03}$) and 33 U and 64 O atoms for UO_{2-x} (producing $\text{UO}_{1.94}$)

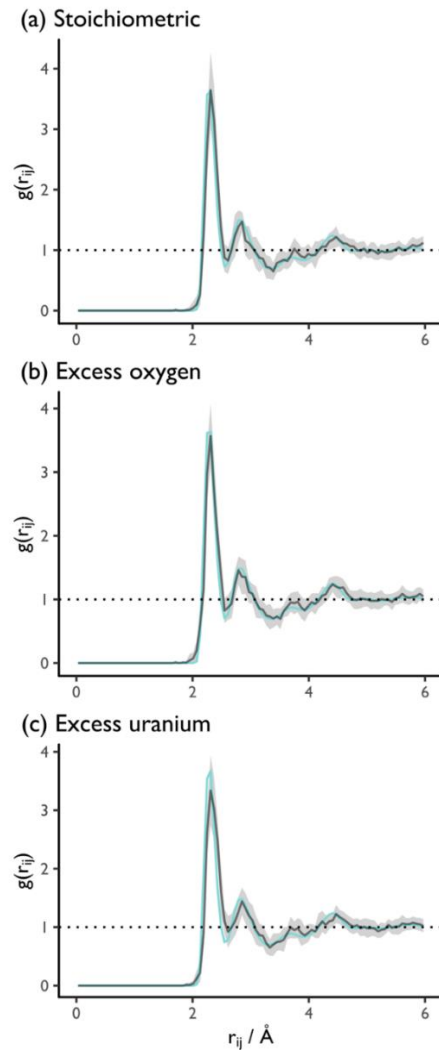


Figure 3 - Radial distribution functions derived from RMC+DFT optimised cells at three different levels of stoichiometry.

The dark grey line shows the RDF obtained as the mean and the surrounding, light grey halo, indicates one standard deviation above and below for the 20 individual DFT configurations for each atomic separation and stoichiometry. For comparison, the blue line is the equivalent molecular dynamics melt-quenched system

A simulated X-ray diffraction pattern was produced by combining the patterns of the 20 stoichiometric UO_2 structures and compared to both the X-ray diffraction pattern of the quenched MD structure and the experimental pattern by Bruno *et al.* [7] and an ideal UO_2 diffraction pattern (Figure 4). It can be seen that the simulated patterns match well with the experimental X-ray diffraction pattern indicating the methodology is suitable to study the system.

The major (111) peak and the (200) peak associated with the crystalline structure local/intermediate fluorite ordering are largely retained in all patterns (a slight inflection is evident at $\sim 32^\circ$ in the MD simulated amorphous UO_2 structure). The MD shows a broad peak at $\sim 50^\circ$ encompassing the smaller peaks evident in this region in the crystalline UO_2 pattern. Some evidence of these peaks is shown in the simulated amorphous DFT structure and the experimental amorphous UO_2 structure.

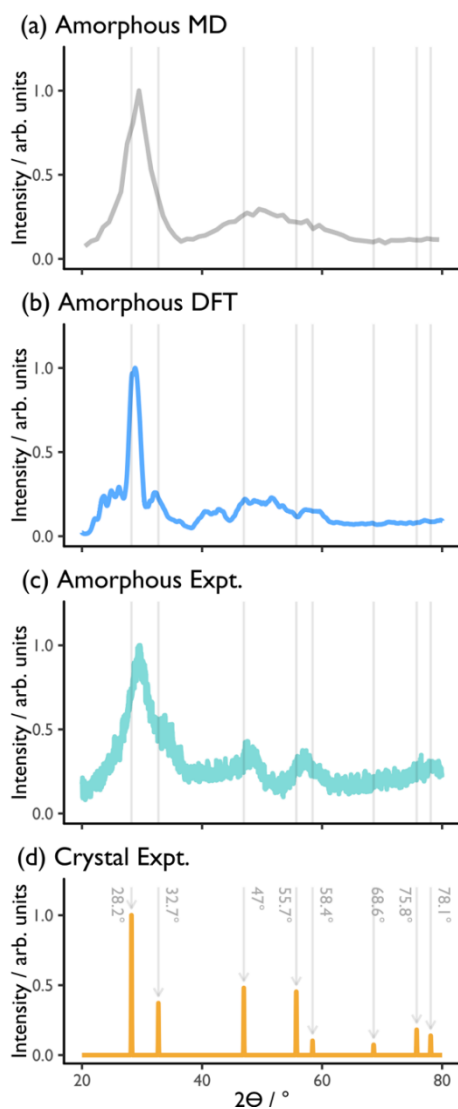


Figure 4 – X-ray diffraction patterns for (a) simulated amorphous UO_2 – MD, (b) simulated amorphous UO_2 – DFT, (c) experimental amorphous UO_2 [7] and (d) experimental crystalline UO_2 [44]. Grey lines are added to all patterns that correspond to the experimental crystalline UO_2 peaks.

By closely comparing the pair-correlation functions from Figure 2 with the bond-angle distributions given in Figure 5 a good picture of the amorphous structure can be gained. This understanding can be further improved by considering the structural features found in the amorphous structure relate to the fluorite crystal structure, as there are clear similarities and crucial differences between these two forms of UO_2 .

First it is instructive to revisit the individual correlation functions for the O-U, O-O and U-U pairs in Figure 2(b)-(d). These have been overlaid with drop-lines showing the position of the relevant 1st, 2nd and 3rd nearest neighbour pair distances in fluorite. For the O-U distribution the amorphous peak positions correspond well with their equivalent fluorite pair distances. The first amorphous peak is at 2.31Å, which is a slight contraction from the first neighbour distance in the crystal which is 2.37Å. This indicates that the same basic building blocks describe both structures – namely OU_4 tetrahedra. It

would not, however, be correct to say that these coordination polyhedra are identical in the two structures. This is shown by the differences in the U-O-U bond angle distributions in Figure 5(a), where the light grey trace was obtained from MD runs for fluorite at T=300K and the dark grey line is for amorphous UO₂ at the same temperature. The distribution for the crystal shows a single peak centred at 109.47° which is consistent with regular tetrahedra. Although the modal value of the U-O-U distribution (dark grey) is close to this value it is smaller than 109.47° and the distribution is now bimodal with a significant shoulder at higher angles (least squares gaussian peak fitting to the distribution predicts positions of 101.74° and 130.78° for these two peaks). This change indicates some distortion to the tetrahedra in the amorphous structure. The reason for this will now be considered.

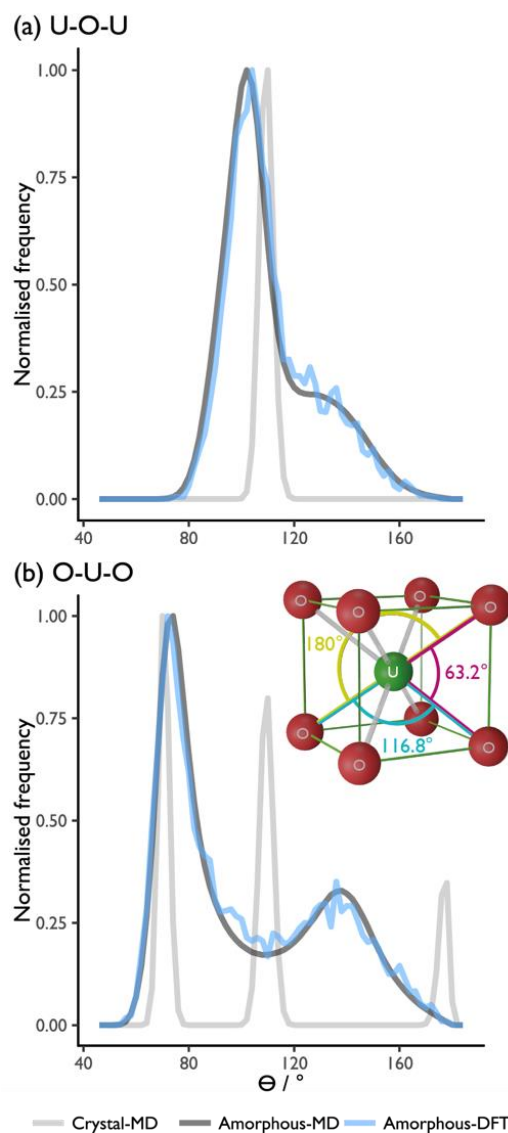


Figure 5 - Bond angle distributions for amorphous UO₂ compared with fluorite crystal. The distribution of angles for (a) U-O-U and (b) O-U-O triplets are shown (inset: representation of uranium coordination environment in crystalline UO₂). The dark grey line shows the distributions for MD melt-quenched systems. The light grey line was obtained from a crystalline, fluorite, structure equilibrated using MD. Both are for a temperature of 300K. The blue line shows the angular distributions

averaged over the 20 RMC+DFT optimised structures. For the purposes of comparison, each distribution has been normalised to have a maximum peak height of 1.0.

As mentioned earlier, the amorphous structure is a network of edge-sharing OU_4 tetrahedra. In which the shared edges run between the uranium atoms shared by two tetrahedra with the edges straddled by the anions of each polyhedron. This arrangement gives rise to a distinctive diamond arrangement also seen in fluorite and highlighted in Figure 6. In the crystal this anion spacing is 2.73\AA at $T=300\text{K}$, however from the first-peak position in Figure 2(c) it can be seen that anions sit slightly further apart (2.85\AA) in the amorphous case. Given that the O-U bond distance remains fundamentally unchanged this lower anion density is partially accommodated through the changes in the U-O-U bond angle. Due to the geometry of the UO_4 tetrahedron, the larger O-O separation across the shared edge causes the O-U bonds describing the diamond shape to rotate (as shown in Figure 6). As this happens, the U atoms at either end of the edge converge, leading to a shorter edge and smaller U-U distance. This effect is apparent in Figure 2(d) where the first peak of the U-U pair correlation function has been shifted to the left of the fluorite first neighbour line. This does not tell the full story, however as the geometry of the UO_4 polyhedron means that shortening one edge leads to a concomitant increase in the other edges with which it shares vertices. Or when described in terms of bond angles as one U-O-U triplet is pinched to a more acute angle this will tend to increase the angle between connected pairs U-O of bonds, in a way that is analogous to the opening of a pair of scissors. This gives rise to the bimodal U-O-U bond angle distribution as the angles split into groups of pinched and stretched angles. Similarly, the first peak of the U-U pair correlation function, Figure 2(d), shows a clear shoulder; a least squares peak fit using two Lorentzian functions indicates two populations of U-U lengths around values of 3.69\AA and 4.22\AA (for reference the length in fluorite for the same temperature is 3.87\AA).

Another feature to note from the relaxations is that the volume per unit is increased by 12.7 % compared to the experimental fluorite UO_2 structure - 46.1 \AA^3 per UO_2 unit giving a density of 9.73 g/cm^3 in the amorphous system versus 40.9 \AA^3 per UO_2 unit in the experimental crystalline UO_2 with corresponding density of 10.97 g/cm^3 [44] (the predicted density of UO_2 through the DFT methods is 10.54 g/cm^3 [45]). This value is similar to that of other related systems including zircon (which has a volume increase upon amorphization of 18.4%) [46] [47] and quartz (where the volume increase is 14 %) [48].

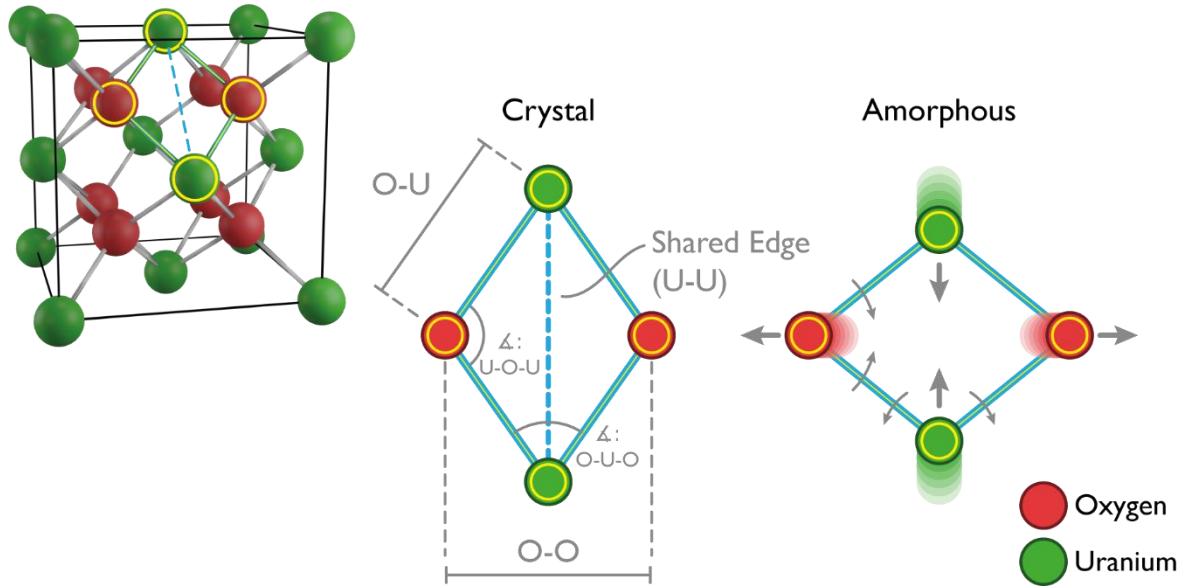


Figure 6 The diamond shape found where two UO_4 tetrahedra share an edge is prevalent in both the crystalline and amorphous forms of UO_2 . Understanding the slight distortion of this feature due to the larger O-O distance in the amorphous phase helps interpret the bond angle distributions and pair-correlation functions.

3.2 Stoichiometry deviation

The energy to accommodate deviations in oxygen stoichiometry in amorphous UO_2 were considered and compared to those in crystalline UO_2 . As examined in previous studies [45], the ease with which the material deviates its stoichiometry with respect to oxygen gas (O_2) is considered [45] [42]. A single extra oxygen was added to produce the UO_{2+x} structure ($U_{32}O_{65}$) and one uranium was added to produce a UO_{2-x} structure ($U_{33}O_{64}$). These reactions are described below:

$$\text{Energy to absorb } \frac{1}{2} O_2 \text{ (red data in Figure 7): } E_{\text{Hyper}}^F = E_{\text{Hyper}}^{U_{32}O_{65}} - E_{\text{Stoich}}^{U_{32}O_{64}} - \frac{1}{2} E_{O_2} \quad (1)$$

$$\text{Energy to produce } \frac{1}{2} O_2 \text{ (blue data in Figure 7): } E_{\text{Hypo}}^F = \frac{1}{2} \left(E_{\text{Hypo}}^{U_{33}O_{64}} - \frac{33}{32} E_{\text{Stoich}}^{U_{32}O_{64}} + E_{O_2} \right) \quad (2)$$

Figure 7 – The computed reaction energies to accommodate a deviation in oxygen stoichiometry in amorphous uranium oxide (as computed by DFT using equations 1 and 2). Histograms (bars) indicate the energies computed and associated kernel density plots (continuous lines) are included to highlight the trend. reports the spread in the energies to accommodate deviations in stoichiometry. As expected in an amorphous system, there is a significant variation in the energy to accommodate deviations in stoichiometry. It is clear that a large proportion of structures show an exothermic reaction energy to accommodate excess oxygen into the amorphous UO_2 structure – indicating that if available, the material will accommodate excess oxygen to become hyper-stoichiometric. Conversely, release of oxygen from amorphous UO_2 is endothermic and therefore under standard conditions, the material is not likely to release oxygen.

Dorado *et al.* [49] computed the formation enthalpy of an oxygen interstitial and vacancy in crystalline UO_2 with respect to O_2 gas. The oxygen interstitial formation energy was computed to be -0.05 eV per O_i , directly comparable with the hyper-stoichiometric data in Figure 7 (red line), and the oxygen vacancy was computed to be 5.30 eV per V_O , comparable to the hypo-stoichiometric data in Figure 7 (blue line). In both cases, the propensity for stoichiometry deviation is more readily accommodated in the amorphous structure computed in this work indicating that if an amorphous phase were present, it would get the deviations in stoichiometry preferentially over the crystalline UO_2 material. The average energy to deviate to a higher O:U ratio (hyper-stoichiometric) was computed to be -1.65 eV per $\frac{1}{2}\text{O}$ and to move to a lower O:U ratio (hypo-stoichiometric) was computed to be 3.77 eV (similar values of -1.92 eV and 3.79 eV were computed for the collinear calculations, indicating only a minor impact for these reactions). In other words, amorphous grain boundary phases in a crystalline matrix would preferentially accommodate non-stoichiometry leaving crystalline UO_2 grains in the matrix. The impact of this result for nuclear fuel operation and behaviour could be significant as changes in bulk stoichiometry impact many properties including fission gas diffusion [50], secondary phase formation [51] [52] [53], the material's melting point [54] and more.

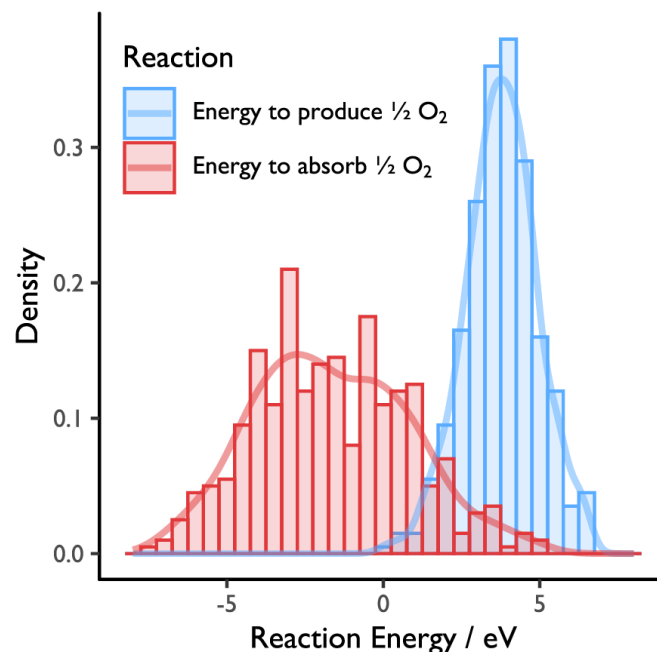


Figure 7 – The computed reaction energies to accommodate a deviation in oxygen stoichiometry in amorphous uranium oxide (as computed by DFT using equations 1 and 2). Histograms (bars) indicate the energies computed and associated kernel density plots (continuous lines) are included to highlight the trend.

3.3 Properties

3.3.1 Magnetic structure and charge

An important result of the present work is that all amorphous structures simulated using DFT (stoichiometric and non-stoichiometric) displayed strong ferromagnetic ordering when simulated using collinear simulations were performed, however when non-collinear effects were considered, a spin-glass type magnetic structure was achieved (speromagnetic). A representative stoichiometric amorphous cell is provided in Figure 8 reporting the direction of the magnetic moments of the U ions in the system (the length indicates the magnitude of the magnetic moment).

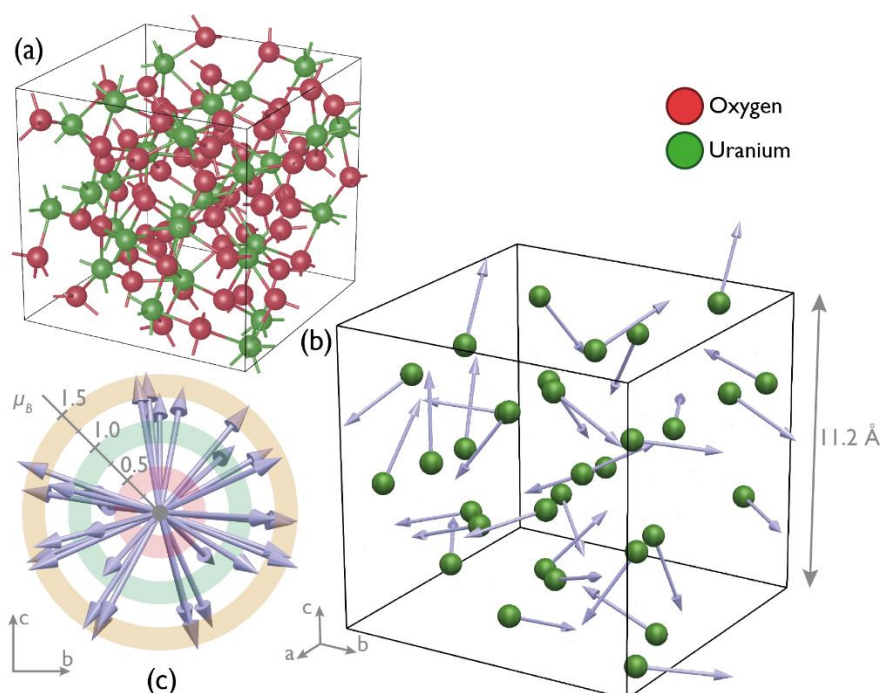


Figure 8 - An example of the magnetic moments in an amorphous UO_2 structure: (a) amorphous structure, (b) magnetic moment vectors for uranium atoms in this structure, (c) parallel projection of vectors when translated to have a common origin.

In the collinear calculations, stoichiometric UO_2 , each U has a magnetic moment of $\sim 2 \mu_B$, while the sub-stoichiometric, UO_{2-x} , system 4 or the 32 U ions had an increased magnetic moment of $\sim 3 \mu_B$ and the opposite was observed for the hyper-stoichiometric, UO_{2+x} , system where two U atoms in each supercell had a magnetic moment of $\sim 1 \mu_B$ (note the remainder of the U ions had a magnetic moment of $\sim 2 \mu_B$ in both non-stoichiometric systems). This indicates that the excess oxygen is accommodated through the oxidation of two U^{4+} ions to U^{5+} ions (charge balancing the additional O^{2-} species) while the reduction in oxygen is accommodated by the formation of two charge balancing U^{3+} ions per oxygen removed from the system. The magnitude of the magnetic moments in the non-collinear simulations were similar to those in the collinear systems: all of the U cations were found to have a moment of $\sim 1.5 \mu_B$ in the stoichiometric and non-stoichiometric systems. In the non-collinear UO_{2-x}

systems, four U ions were found with a higher $\sim 2.5 \mu_B$ moment and in the UO_{2+x} system two U ions were found with a lower $\sim 0.8 \mu_B$ moment. The magnetic moment for all 20 systems was $1.35 \mu_B$ (i.e. close to negligible), highlighting the spin-glass/speromagnetic nature of the system. Bader charge analysis was carried out [55] [56] [57] to confirm the changes in charge on the U atoms consistent with the magnetic moment – ions that showed deviations in magnetic magnitude in the non-stoichiometric cells were observed to either be in a higher or lower charge state ($\sim \pm 0.3e$) depending on the system in agreement with taking a 3+ and 5+ formal charge.

The change in charge in the non-stoichiometric systems can be seen in slight changes in the cation coordination environment for each stoichiometry. In Figure 9, it can be seen that the presence of the smaller U^{5+} cation in the UO_{2+x} system is evident by a closer U-O distance for these specific species. Conversely, in the UO_{2-x} system, the U-O distance is extended slightly accounting for the slightly larger ionic radius of the U^{3+} . Additionally, the coordination environment of the charge compensating uranium cations, although similar, is distinct from the majority of the cations in the system, that share the same charge state as found in the stoichiometric system and are represented by the U^{4+} -O lines (orange) in Figure 9.

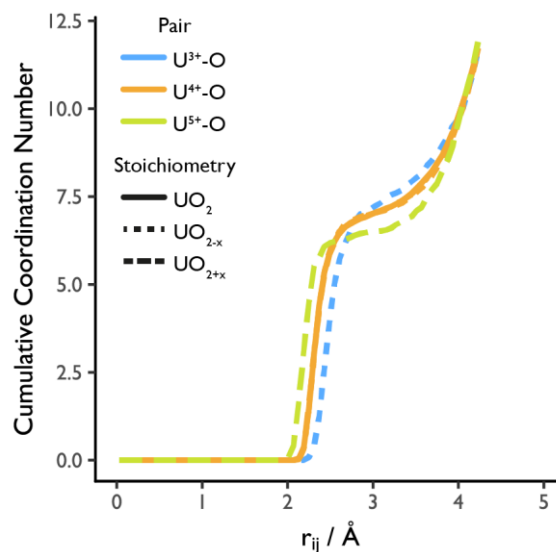


Figure 9 Coordination number surrounding uranium cations with different charge states, as determined by Bader analysis. The cumulative coordination number was obtained by integrating the U-O pair correlation functions of each U species for the three stoichiometries considered as a function of separation. It should be noted that the U^{4+} -O trace overlaps almost completely for the UO_2 , UO_{2+x} and UO_{2-x} cases giving the appearance of single line.

Crystalline uranium dioxide is known to be anti-ferromagnetic with a Néel temperature of 30.8 K, however, it has been observed that weak ferromagnetism can be induced by doping UO_2 with largely insoluble oxides including TiO_2 and SiO_2 [58] [59]. Nakamura *et al.* [59] proposed that the ferromagnetism could be due to near surface effects when the dopant species distorts the lattice. In addition to this plausible impact, the result from this investigation highlights the potential for an

amorphous phase (potentially stabilized by impurities/dopants such as TiO_2 and SiO_2) at the grain boundaries inducing the weak deviation in magnetic behaviour. This indicates that the addition of certain dopants (both Ti and Si have been used to increase grain size and impact fission gas release [60] [61]) may function partly by inducing an amorphous phase that accelerates grain growth during sintering. Future work will assess the stabilization of amorphous phases by these and other dopants/impurities, understanding the potential for behaviour such as speromagnetism and asperomagnetism [62] in these amorphous systems and the broader impact of the spin-glass behaviour related to experimental observations.

3.3.2 Surface energy

The surface energy was simply computed as the difference in energy between the bulk amorphous structure and the surface structure divided by total area of the surfaces generated (converting to give a value in Jm^{-2}). An example surface simulation cell is illustrated in Figure 10. Only collinear calculations were used due to the computational expense. The similarity between the collinear and non-collinear defect values for the oxygen defect accommodation reactions in section 3.2 provide some assurance that the energies are reasonable, but future work should consider the surface energies with the non-collinear model.

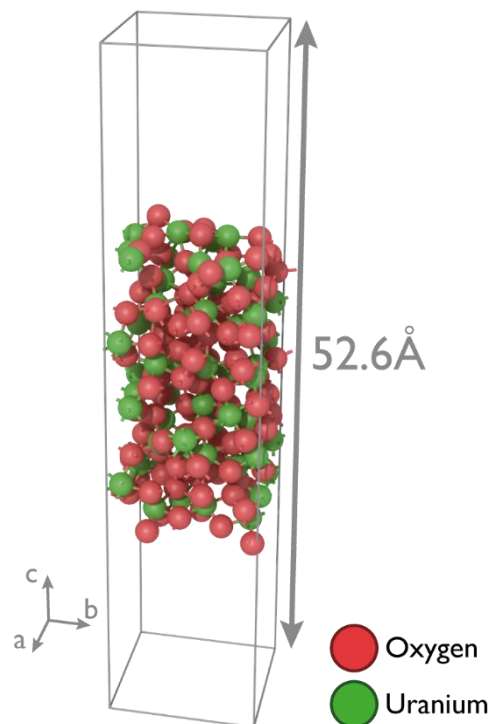


Figure 10 - Example cell used to compute the surface energy of amorphous UO_2 . Two surfaces are created (upper and lower) with a vacuum gap (30 \AA) separating them.

The average surface energy of the 20 surfaces produced with respect to the bulk material was 0.79 Jm^{-2} with a standard deviation of 0.14 Jm^{-2} . Further work to optimise the computation is required, but it is encouraging that other experimental values for related amorphous oxide systems are

similar to this value, for example amorphous Al_2O_3 with an energy of $0.97 \pm 0.04 \text{ Jm}^{-2}$ [63], and amorphous HfO_2 nanoparticles with surface energies of 0.76 ± 0.12 , 0.47 ± 0.2 , and $0.59 \pm 0.1 \text{ Jm}^{-2}$, depending on the measurement technique used [64]. The calculated surface energy of the (111) surface in crystalline UO_2 was previously calculated to be 0.8 Jm^{-2} by Evarestov *et al.* [65] and 0.76 - 0.78 Jm^{-2} calculated by Weck *et al.* [66] (generally lower than the energies computed using rigid charge empirical potentials with values between 0.89 - 1.48 Jm^{-2} [67]).

The experimental value of surface energy in UO_2 reported by Hall *et al.* [68] is 0.85 Jm^{-2} , similar to both the calculated (111) surface energy and the amorphous surface energy calculated here, although the reported experimental errors are extremely large ($\sim 70\%$). Given the importance of the prediction of surface energy on fuel performance characteristics such as intergranular fission gas bubble formation [69] [70], gas mobility and release [71], fuel fragmentation [72] [73] [74] and more, it is clear that the impact of amorphous grain boundary formation (including the need to consider extrinsic species such as fission products in high concentrations [75] [76] [77]) should be considered.

4. Summary

Atomistic simulations have been carried out investigating amorphous UO_2 , linking empirical potential-based calculations utilizing molecular dynamics methods, with density functional theory (DFT)-based simulations to get a multi-scale description of the system for the first time. The structures of the amorphous UO_2 systems predicted by the molecular dynamics methods and subsequent DFT-relaxed structures are consistent with each other and their predicted X-ray diffraction pattern is consistent with the experimentally attained pattern [7].

Although the methods used in this investigation have previously been used to assess amorphous oxides on the atomic scale [34], here the impact that the size of the initial molecular dynamics melt-quench simulations has on the final structure was also investigated. These simulations highlight far more units than can be routinely simulated using density functional theory methods, here well over 256 units of UO_2 were required to ensure an amorphous structure is produced through the thermal treatment employed.

Bond angles in the amorphous system were predicted and compared to the crystalline UO_2 structure where it was found that both the U-O-U and O-U-O angles show similarities with the local structure of the crystalline structure but deviate for angles expected for species at higher separations.

Non-stoichiometry in amorphous UO_2 has been considered, and it is predicted that the amorphous structure can deviate to UO_{2+x} and UO_{2-x} more readily than the crystalline form. As such, it is expected that any amorphous UO_2 regions in nuclear fuel (formed during operation or as a result of

manufacture processes) could act as getters for deviations in stoichiometry resulting from its operation. The preferential accommodation of non-stoichiometry by grain boundaries in other materials has been considered in past work [78] and the gettering of deviations to stoichiometry by grain boundary phases would impact the in-reactor behaviour of fuel as bulk transport, structure, thermo-chemical and thermo-mechanical bulk properties are all affected by the O/U ratio in single effects studies. In this respect, further work is required to ascertain the impact of known impurity/dopant species in stabilizing amorphous grain boundary phases including those highlighted by Solomon *et al.* [13]. The impact that the grain boundary phases may have on fission product behaviour, including those of fission gases that impact fuel performance, as well as mechanical properties including the effects of deviations to grain boundary creep/deformation will be of significant interest to the nuclear fuel community and beyond.

As non-collinear spin-polarized DFT calculations were considered, the magnetic ordering of the amorphous UO_2 system was predicted. Unlike crystalline UO_2 at 0 K, which is predicted to be anti-ferromagnetic, the amorphous system shows a random spin structure consistent with a spin-glass. Future work will consider the potential for dopants and impurities have to induce ferromagnetic-like behaviour (asperomagnetic) that may correlate with experimental observations [59]. Further work should again be considered to ascertain the role of impurities in stabilizing amorphous UO_2 .

Lastly, the surface energy of amorphous UO_2 was determined and compared to surface energies in crystalline UO_2 . The average energy of 0.79 Jm^{-2} is similar to the surface energies reported in the crystalline structure. The methodology used to compute the surface energy (combining the use of DFT and empirical interatomic potentials) has been described in full and shall be used as the basis of future developments to optimise the prediction of this value. Recent work by Ksibi *et al.* [11] re-stated the long-held importance of understanding grain boundary bubble behaviour noted from the inception of nuclear fuel performance modelling [79] [80], here we begin to consider the potential atomic scale behaviour of non CSL boundaries.

5. Acknowledgments

SCM, WEL and MJDR are funded through the Sêr Cymru II programme by Welsh European Funding Office (WEFO) under the European Development Fund (ERDF). Computing resources were made available by Supercomputing Wales.

6. References

- [1] J. Arborelius, K. Backman, L. Hallstadius, M. Limback, J. Nillson, B. Rebensdorff, G. Zhou, K. Kinato, R. Lofstrom and G. Ronnberg, Advanced doped UO_2 pellets in LWR applications, J. Nucl. Sci. Technol. 43 (2006) 967-976,.

- [2] R. Yuda, H. Harada and M. Hirai, Effects of pellet microstructure on irradiation behavior of UO₂ fuel, *J. Nucl. Mater.* 248 (1997) 262-267,.
- [3] J.B. Ainscough, F. Rigby and S.C. Osborn, The effect of titania on grain growth and densification of sintered UO₂, *J. Nucl. Mater.* 52 (1974) 191-203,.
- [4] B.J. Jaques, J. Watkins, J.R. Croteau and G.A. Alanko, Synthesis and sintering of UN-UO₂ fuel composites, *J. Nucl. Mater.* 466 (2015) 745-754.
- [5] S. Nishigaki and K. Maekawa, Fabrication of BeO-UO₂-Be fuel pellets, *J. Nucl. Mater.* 14 (1964) 453-458.
- [6] H. Matzke, V. Nitzki and C. Ronchi, The crystallisation of amorphous UO₂, *Thin Solid Films* 22 (1974) 75-82.
- [7] J. Bruno, I. Casas, B. Lagerman and M. Munoz, The Determination of the Solubility of amorphous UO₂ (S) and the mononuclear hydrolysis constants of uranium(IV) at 25° C, *Mater. Res. Soc. Symp. Proc.* 84 (1986) 153.
- [8] S. Dillon, M. Tang, W. Carter and M. Harmer, Complexion: A new concept for kinetic engineering in materials science, *Acta Mater.* 55 (2007) 6208-6218.
- [9] P.R. Cantwell, M. Tang, S.J. Dillon, J. Luo, G.S. Rohrer and M.P. Harmer, Grain boundary complexions, *Acta Mater.* 62 (2014) 1-48.
- [10] H. Grimmer, W. Bollmann and D. Warrington, Coincidence-site lattices and complete pattern-shift in cubic crystals, *Acta Cryst.* 30 (1974) 197-207.
- [11] A. Ksibi, E. Bourasseau, X. Iltis, D. Drouan, M. Gaudet, A. Germain, P. A., G. Lapertot, J-P. Brison and R.C. Belin, Experimental and numerical assessment of grain boundary energies in polycrystalline uranium dioxide, *J. Eur. Ceram.* Accepted in press, doi:<https://doi.org/10.1016/j.jeurceramsoc.2020.04.041>, 2020.
- [12] E. Bourasseau, A. Mouret, P. Fantou, X. Iltis and R.C. Belin, Eperimental and simulation study of grain boundaries in UO₂, *J. Nucl. Mater.* 517 (2009) 286-295.
- [13] A.A. Solomon, C.S. Yust and N.H. Packan, Primary creep of UO₂ and the effect of amorphous grain boundary phases, *J. Nucl. Mater.* 110 (1982) 333-342.
- [14] M.J.D. Rushton, R.W. Grimes and S.L. Owens, Predicted Changes to Alkali Concentration Adjacent to Glass–Crystal Interfaces, *J. Am. Ceram. Soc.* 91 (2008) 1659-1664.
- [15] T.R. Stechert, M.J.D. Rushton, R.W. Grimes and A.C. Dillon, Predicted structure, thermo-mechanical properties and Li ion transport in LiAlF₄ glass, *J. Non-Cryst. Solids* 358 (2012) 1917.
- [16] T.G. Desai, P. Nerikar and B.P. Uberuaga, The role of grain boundary structure in stress-induced phase transformation in UO₂, *Model. Simul. Mater. Sci.* 17 (2009) 064001.
- [17] M.J. Qin, M.W.D. Cooper, E.Y. Kuo, M.J.D. Rushton, R.W. Grimes, G.R. Lumpkin and S.C. Middleburgh, Thermal conductivity and energetic recoils in UO₂ using a many-body potential model, *J. Phys. Condens. Matter* 26 (2014) 459401.

- [18] M.W.D. Cooper, M.J.D. Rushton and R.W. Grimes, A many-body potential approach to modelling the thermomechanical properties of actinide oxides, *J. Phys. Condens. Matter* 26 (2014) 105401.
- [19] D. Vanderbilt, X. Zhao and D. Ceresoli, Structural and dielectric properties of crystalline and amorphous ZrO_2 , *Thin Solid Films* 486 (2005) 125-128.
- [20] D. Ceresoli and D. Vanderbilt, Structural and dielectric properties of amorphous ZrO_2 and HfO_2 , *Phys. Rev. B* 74 (2006) 125108.
- [21] E. Chagarov and A. Kummel, Generation of Realistic Amorphous Al_2O_3 And ZrO_2 Samples By Hybrid Classical and First-Principle Molecular Dynamics Simulations, *ECS Trans.* 16 (2008).
- [22] D.M. Ramo, A. Chroneos, M.J.D. Rushton and P.D. Bristowe, Effect of trivalent dopants on local coordination and electronic structure in crystalline and amorphous ZnO , *Thin Solid Films* 555 (2014) 117-121.
- [23] A. Pandey, H. Scherich and D.A. Drabold, Density functional theory model of amorphous zinc oxide ($a-ZnO$) and $a-X_{0.375}Zr_{0.625}O$ ($X= Al, Ga$ and In), *J. Non-Cryst. Solids* 455 (2017) 98-101.
- [24] M. Durandurdu, Amorphous zirconia: ab initio molecular dynamics simulations, *Philos. Mag.* 97 (2017) 1334-1345.
- [25] D. Mora-Fonz and A. Shluger, Making amorphous ZnO : Theoretical predictions of its structure and stability, *Physical Rev. B* 99 (2019) 014202.
- [26] P.R. Laurence and I.H. Hillier, Towards modelling bioactive glasses: Quantum chemistry studies of the hydrolysis of some silicate structures, *Comput. Mat. Sci.* 28 (2003) 63-75.
- [27] M. Corno, A. Pedone, R. Dovesi and P. Ugliengo, B3LYP Simulation of the Full Vibrational Spectrum of 45S5 Bioactive Silicate Glass Compared to v -Silica, *Chem. Mater.* 20 (2008) 5610-5621.
- [28] A. Pedone, T. Charpentier and M. Menziani, The structure of fluoride-containing bioactive glasses: new insights from first-principles calculations and solid state NMR spectroscopy, *J. Mater. Chem.* 22 (2012) 12599.
- [29] J.K. Christie, A. Pedone, M.C. Menziani and A. Tilotta, Fluorine Environment in Bioactive Glasses: ab Initio Molecular Dynamics Simulations, *J. Phys. Chem. B* 115 (2011) 2038-2045.
- [30] R.M. Van Ginhoven, H. Jonsson and L.R. Corrales, Silica glass structure generation for ab initio calculations using small samples of amorphous silica, *Physical Rev. B* 71 (2005) 024208.
- [31] J. Du, L. Corrales, K. Tsemekhman and E. Bylaska, Electron, hole and exciton self-trapping in germanium doped silica glass from DFT calculations with self-interaction correction, *Nucl. Instrum. Meth B* 255 (2007) 188-194.
- [32] N.B.A. Thompson, S.C. Middleburgh, L.J. Evitts, M. Gilbert, M. Stennet and N. Hyatt, Short communication on further elucidating the structure of amorphous U_2O_7 by extended X-ray absorption spectroscopy and DFT simulations, *J. Nucl. Mat.* 542 (2020) 152476.
- [33] D.J.M. King, S.C. Middleburgh, A. Liu, H. Tahini, G. Lumpkin and M. Cortie, Formation and structure of V-Zr amorphous alloy thin films, *Acta Mater.* 83 (2015) 269-275.

- [34] M.J.D. Rushton, I. Ipatova, E.J. Evitts, W.E. Lee and S.C. Middleburgh, Stoichiometry deviation in amorphous zirconium dioxide, *RSC Adv.* 9 (2019) 16320-16327.
- [35] R. L. McGreevy and L. Pusztai, Reverse Monte Carlo Simulation: A New Technique for the Determination of Disordered Structures, *Mol. Simulat.* 1 (1988) 359.
- [36] G. Kresse and J. Hafner, Ab initio molecular dynamics for liquid metals, *Physical Rev. B* 47 (1993) 558.
- [37] J.P. Perdew, K. Burke and M. Ernzerhof, Generalized Gradient Approximation Made Simple, *Physical Rev. Lett.* 77 (1996) 3865.
- [38] P.E. Blöchl, Projector augmented-wave method, *Physical Rev. B* 50 (1994) 17953.
- [39] B. Dorado, B. Amadon, M. Freyss and M. Bertolus, DFT+U calculations of the ground state and metastable states of uranium dioxide, *Physical Rev. B*, 79 (2009) 235215.
- [40] A.I. Liechtenstein, V.I. Anisimov and J. Zaanen, Density-functional theory and strong interactions: Orbital ordering in Mott-Hubbard insulators, *Physical Rev. B* 52 (1995) R5467.
- [41] S.C. Middleburgh, I. Ipatova, L.J. Evitts, M.J.D. Rushton, B. Assinder, R.W. Grimes and W.E. Lee, Evidence of excess oxygen accommodation in yttria partially-stabilized zirconia, *Scr. Mater.* 175 (2020) 7-10.
- [42] S.C. Middleburgh, G.R. Lumpkin and R.W. Grimes, Accommodation of excess oxygen in fluorite dioxides, *Solid State Ionics* 253 (2013) 119-122.
- [43] S.C. Middleburgh, I. Karatchevtseva, B.J. Kennedy, P.A. Burr, Z. Zhang, E. Reynolds, R.W. Grimes and G.R. Lumpkin, Peroxide defect formation in zirconate perovskites, *J. Mater. Chem. A* 2 (2014) 15883-15888.
- [44] L. Desgranges, G. Baldinozzi, G. Rousseau, J-C. Niepce and G. Calvarin, Neutron Diffraction Study of the in Situ Oxidation of UO₂, *Inorg. Chem.* 48 (2009) 7585-7592.
- [45] B. Dorado, G. Jomard, M. Freyss and M. Bertolus, Stability of oxygen point defects in UO₂ by first-principles DFT+U calculations: Occupation matrix control and Jahn-Teller distortion, *Physical Rev. B* 82 (2010) 035114.
- [46] S. Rios, E. Salje, M. Zhang and R.C. Ewing, Amorphization in zircon: evidence for direct impact damage, *J. Phys. Condens. Matter* 12 (2000) 2401.
- [47] W.J. Weber, Radiation-induced defects and amorphization in zircon, *Mater. Res.* 5 (1990) 2687-2697.
- [48] L.W. Hobbs, The role of topology and geometry in the irradiation-induced amorphization of network structures, *J. Non-Cryst. Solids* 182 (1995) 27-39.
- [49] B. Dorado, First-principles calculation and experimental study of oxygen diffusion in uranium dioxide, *Physical Rev. B* 83 (2011) 035126.
- [50] W. Miekeley and F. Felix, Effect of stoichiometry on diffusion of xenon in UO₂, *J. Nucl. Mater.* 42 (1972) 297-306.

- [51] Hj. Kleykamp, The chemical state of fission products in oxide fuels at different stages of the nuclear fuel cycle, *Nucl. Technol.* 80 (1988) 412-422.
- [52] S.C. Middleburgh, D.C. Parfitt, R.W. Grimes, B. Dorado, M. Bertolus, P.R. Blair, L. Hallstadius and K. Backman, Solution of trivalent cations into uranium dioxide, *J. Nucl. Mater.* 420 (2012) 258-261.
- [53] M.W.D Cooper, S.C. Middleburgh and R.W. Grimes, Partition of soluble fission products between the grey phase, ZrO_2 and uranium dioxide, *J. Nucl. Mater.* 438 (2013) 238-245.
- [54] D. Manara, C. Ronchi and M. Sheindlin, Solidus and liquidus of UO_{2+x} from high-pressure melting experiments, *High Temp.-High Press.* 35/36 (2003) 25-33.
- [55] W. Tang, E. Sanville and G. Henkelman, A grid-based Bader analysis algorithm without lattice bias, *Phys. Condens. Matter* 21 (2009) 084204.
- [56] E. Sanville, S.D. Kenny, R. Smith and G. Henkelman, An improved grid-based algorithm for Bader charge allocation, *J. Comp. Chem.*, 28 (2007) 899-908.
- [57] G. Henkelman, A. Arnaldsson and H. Jónsson, A fast and robust algorithm for Bader decomposition of charge density, *Comput. Mater. Sci.* 36 (2006) 354-360.
- [58] A. Nakamura, S. Tsutsui and K. Yoshiic, Antiferromagnetic–ferromagnetic crossover in UO_2 – TiO_x multi-phase systems, *J. Magn. Magn. Mater.* 226-230 (2001) 876-878.
- [59] A. Nakamura and K. Yoshii, Weakferromagnetism induced in UO_2 - MO_x heterogeneous multi-phase systems ($M = Ti, Nb, Si, V$; etc.), *J. Nucl. Sci. Technol.* 39 (2002) 160-163.
- [60] Hj. Matzke, On the effect of TiO_2 additions on sintering of UO_2 , *J. Nucl. Mater.* 20 (1966) 328-331.
- [61] S. Kashibe and K. Une, Effect of additives ($Cr_2O_3, Al_2O_3, SiO_2, MgO$) on diffusional release of ^{133}Xe from UO_2 fuels, *J. Nucl. Mater.* 254 (1998) 234-242.
- [62] J.M.D. Coey, Amorphous magnetic order, *J. Appl. Phys.* 49 (1978) 1646.
- [63] A.H. Tavakoli, P.S. Maram, S.J. Widgeon and J. Rufner, K. van Benthem, S. Ushakov, S. Sen, A. Navrotsky, Amorphous alumina nanoparticles: Structure, surface energy and thermodynamic phase stability, *J. Phys. Chem. C* 117 (2013) 17123-17130.
- [64] G. Sharma, S. Ushakov, H. Li, R. Castro and A. Navrotsky, Calorimetric Measurements of Surface Energy of Amorphous HfO_2 Nanoparticles Produced by Gas Phase Condensation, *The J. Phys. Chem. C* 121 (2017) 10392-10397.
- [65] R. Evarestov, A. Bandura and E. Blokhin, Surface modelling on heavy atom crystalline compounds: HfO_2 and UO_2 fluorite structures, *Acta Mater.* 57 (2009) 600-606.
- [66] P.F. Weck, E. Kim, C.F. Jove-Colon and D.C. Sassani, On the role of strong electron correlations in the surface properties and chemistry of uranium dioxide, *Dalton Trans.* 42 (2013) 4570.
- [67] M. Abramowski, R.W. Grimes and S. Owens, Morphology of UO_2 , *J. Nucl. Mater.* 275 (1999) 12-18.

- [68] R.O.A. Hall, M.J. Mortimer and D.A. Mortimer, Surface energy measurements on UO_2 - a critical review, *J. Nucl. Mater.* 148 (1987) 237-256.
- [69] J.A. Turnbull and M.O. Tucker, Swelling in UO_2 under conditions of gas release, *Phil. Mag.* 30 (1974) 47-63.
- [70] G. Pastore, L. Luzzi, V. Di Marcello and P. Van Uffelen, Physics-based modelling of fission gas swelling and release in UO_2 applied to integral fuel rod analysis, *Nucl. Eng. Des.* 256 (2013) 75-86.
- [71] M.J.F. Notley and I.J. Hastings, A microstructure-dependent model for fission product gas release and swelling in UO_2 fuel, *Nucl. Eng. Des.* 56 (1980) 163-175.
- [72] K. Une, S. Kashibe and K. Hayashi, Fission Gas Release Behavior in High Burnup UO_2 Fuels with Developed Rim Structure, *J. Nucl. Sci. Technol.* 39 (2002) 668-674.
- [73] K. Une, S. Kashibe and A. Takagi, Fission Gas Release Behavior from High Burnup UO_2 Fuels under Rapid Heating Conditions, *J. Nucl. Sci. Technol.* 43 (2006) 1161-1171.
- [74] Y. Zhang, P.C. Millett, M.R. Tonks, X.M. Bai and S.B. Biner, Molecular dynamics simulations of intergranular fracture in UO_2 with nine empirical interatomic potentials, *J. Nucl. Mater.* 452 (2014) 296-303.
- [75] M. Hong, B.P. Uberuaga, S.R. Phillpot, D.A. Andersson, C.R. Stanek and S.B. Sinnott, The role of charge and ionic radius on fission product segregation to a model UO_2 grain boundary, *J. Appl. Phys.* 113 (2013) 134902.
- [76] N. Oi and J. Takagi, Distribution of Fission Products in Irradiated UO_2 , *J. Nucl. Sci. Technol.* 2 (1965) 127-131.
- [77] N. Oi and I. Tanabe, Fission product segregation at the surface of irradiated UO_2 particles, *J. Nucl. Mater.* 25 (1968) 288-295.
- [78] H. Bail, M. Kim, G.-S. Park, S.A. Song and M. Varela, Interface structure and non-stoichiometry in HfO_2 dielectrics, *Appl. Phys. Lett.* 85 (2004) 672-674.
- [79] G.W. Greenwood and M.V. Speight, An analysis of the diffusion of fission gas bubbles and its effect on the behaviour of reactor fuels, *J. Nucl. Mater.* 10 (1963) 140-144.
- [80] J. Rest and S. Gehl, The mechanistic prediction of transient fission-gas release from LWR fuel, *Nucl. Eng. Des.* 56 (1980) 233-256.
- [81] L. Desgranges, G. Baldinozzi, G. Rousseau, J.-C. Niepce and G. Calvarin, Neutron Diffraction Study of the in Situ Oxidation of UO_2 , *Inorg. Chem.* 48 (2009) 7585-7592.